



Ce_{0.8}Sn_{0.2}O_{2-δ}–C composite as a co-catalytic support for Pt catalysts toward methanol electrooxidation

Yu Gu^a, Chuntao Liu^{a,b,*}, Yabei Li^a, Xulei Sui^c, Kuo Wang^a, Zhenbo Wang^c

^a School of Chemistry and Materials Science, Heilongjiang University, Harbin 150080, China

^b Key Laboratory of Chemical Engineering Process and Technology for High-efficiency Conversion, College of Heilongjiang Province, Harbin 150080, China

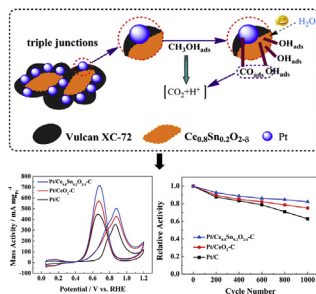
^c School of Chemical Engineering and Technology, Harbin Institute of Technology, Harbin 150001, China



HIGHLIGHTS

- Ce_{0.8}Sn_{0.2}O_{2-δ} solid solution is prepared by a simple one-step solvothermal route.
- Incorporation Sn into CeO₂ enhances its oxygen storage capacity.
- Ce_{0.8}Sn_{0.2}O_{2-δ}–C is used as a co-catalytic hybrid support for Pt electrocatalysts.
- Pt/Ce_{0.8}Sn_{0.2}O_{2-δ}–C catalyst has a triple junction structure (Pt–Ce_{0.8}Sn_{0.2}O_{2-δ}–C).
- Pt/Ce_{0.8}Sn_{0.2}O_{2-δ}–C shows great catalytic properties for methanol electrooxidation.

GRAPHICAL ABSTRACT



ARTICLE INFO

Article history:

Received 1 February 2014

Received in revised form

15 April 2014

Accepted 28 April 2014

Available online 9 May 2014

Keywords:

Direct methanol fuel cells

Sn-doped CeO₂

Electrocatalyst support

Methanol electrooxidation

ABSTRACT

Ce_{0.8}Sn_{0.2}O_{2-δ} solid solution is fabricated using a simple one-step solvothermal method. The synthesized solid solution mixed with Vulcan XC-72 carbon black (denoted by Ce_{0.8}Sn_{0.2}O_{2-δ}–C) is employed as a co-catalytic support for Pt catalysts toward methanol electrooxidation. X-ray diffraction (XRD), transmission electron microscope (TEM), X-ray photoelectron spectroscopy (XPS), Raman spectroscopy, N₂ adsorption/desorption and temperature programmed reduction (TPR) are used to characterize the properties of Ce_{0.8}Sn_{0.2}O_{2-δ} solid solution. The results show that Ce_{0.8}Sn_{0.2}O_{2-δ} possesses a high specific surface area, an enhanced conductivity and a high oxygen storage capacity (OSC). Pt catalysts grown around Ce_{0.8}Sn_{0.2}O_{2-δ} on carbon black form a special Pt–Ce_{0.8}Sn_{0.2}O_{2-δ}–C triple junction structure, and their electrocatalytic properties are investigated in detail by a series of electrochemical methods. As compared with Pt/CeO₂–C and commercial Pt/C catalysts, Pt/Ce_{0.8}Sn_{0.2}O_{2-δ}–C catalyst exhibits superior electrocatalytic activity and long-term stability for methanol electrooxidation in acid media. The origin of the enhanced electrocatalytic properties for Pt/Ce_{0.8}Sn_{0.2}O_{2-δ}–C is closely related to the OSC of Ce_{0.8}Sn_{0.2}O_{2-δ} and the triple junction structure.

© 2014 Elsevier B.V. All rights reserved.

1. Introduction

Direct methanol fuel cells (DMFCs) are promising power sources for portable electronic devices and electric vehicles due to their high efficiency, low pollution, convenience and practicality [1–4]. In the past decades, considerable efforts have been devoted to

* Corresponding author. School of Chemistry and Materials Science, Heilongjiang University, Harbin 150080, China. Tel.: +86 451 86608549; fax: +86 451 86609521.

E-mail addresses: hdguyu@163.com (Y. Gu), ctliu210@gmail.com (C. Liu).

promoting large-scale commercialization of DMFCs. However, there are still unsolved obstacles greatly hampering its broad applications [5–7]. The main disadvantage of Pt-based catalysts, commonly used as the anode catalysts, is easily poisoned by the intermediate species from the methanol electrooxidation [8–10]. Moreover, the migration and agglomeration of Pt nanoparticles on the carbon support also cause the poor durability of the catalysts over time [11–13]. To overcome these problems, some co-catalytic materials need to be introduced to improve the electrocatalytic performance of Pt catalyst [3,7,14,15]. Among these supports, metal oxides (MOs) combined with carbon materials (MOs–C) have been extensively studied as the hybrid supports because of their excellent properties for improving the performance of Pt catalysts, which mainly present in the following two aspects: (i) the MOs increases the resistance to poisoning effect from CO-like intermediate species [16–21], and (ii) the MOs promotes the dispersion of Pt nanoparticles on hybrid support and mitigates their migration and agglomeration [22–25].

Among the various MOs–C hybrid supports, the CeO₂–C composite has received considerable attention mainly due to the unique characteristic of CeO₂. Xu and Shen [26,27] initially reported the alcohols electrooxidation on Pt–CeO₂/C catalyst in alkaline solution, and observed a significant improvement in the electrode performance in comparison with Pt/C. Ha's group [28] reported that the incorporation of 9 wt.% CeO₂ can promote the catalytic activity and stability of Pt/C catalyst toward methanol electrooxidation via the called bifunctional mechanism. Wang and coworkers [29] reported that the Pt/CeO₂/graphene composites, in which the Pt nanoparticles were deposited around CeO₂ on the graphene to give a triple junction structure, exhibited a remarkably enhanced catalytic performance for methanol electrooxidation. All these reports have shown that Pt catalysts deposited on the CeO₂–C support exhibit not only high dispersion due to the anchoring effect of CeO₂, but also good performance for methanol electrooxidation due to the easy release of poisoning intermediates from Pt surface. The regeneration of poisoned Pt is ascribed to the fact that the OH_{ads} supplied by CeO₂ efficiently promotes the oxidation of poisoning intermediates. The key factor for OH_{ads} generation is the concentration of oxygen vacancies in CeO₂, i.e., the oxygen storage capacity (OSC) of CeO₂. In general, the more oxygen vacancies CeO₂ possesses, the more OH_{ads} CeO₂ provides. However, the concentration of oxygen vacancies in the pure CeO₂ is lower, hence limiting the full development of its co-catalytic action on methanol electrooxidation.

Doping with appropriate dopants can efficiently increase the concentration of oxygen vacancies in CeO₂ [30,31]. The doped CeO₂ with a higher number of oxygen vacancies has shown the better catalytic/co-catalytic performance and higher stability in many catalytic reactions [32–35]. In the field of alcohol electrooxidation, Zr-doped CeO₂ [36] and Pr-doped CeO₂ [37] have been used to improve the CO tolerance of Pt/C catalyst, thus enhancing the performance. However, these reports lack the convective information on the characterization of the crystal structure of doped CeO₂ to some extent. At the same time, the co-catalytic effect of doped CeO₂ is still unclear. Therefore, the related work is expected to be further perfected.

We propose the use of Sn as a dopant to maximize the co-catalytic action of CeO₂ for methanol electrooxidation. Firstly, the redox behavior (Sn⁴⁺/Sn²⁺) of Sn may improve the OSC of CeO₂, which is conducive to CO oxidation during the methanol electrooxidation reaction. Secondly, the addition of Sn into CeO₂ lattice may increase the specific surface area of the composite, which favors better dispersion and anchoring of Pt, and enhances the durability of the catalyst. Finally, Sn may improve the electrical conductivity of CeO₂, which is favorable for the improvement of the electrocatalytic activity of the catalyst.

Based on the above considerations, we have synthesized the Sn-doped CeO₂ solid solution (Ce_{0.8}Sn_{0.2}O_{2-δ}) with a higher OSC, higher surface area and enhanced conductivity through a solvothermal method. Our tests show that the composite of Ce_{0.8}Sn_{0.2}O_{2-δ} and carbon black can be used as support of Pt nanoparticles with the improved electrocatalytic activity and durability for methanol electrooxidation. The structure and properties of Ce_{0.8}Sn_{0.2}O_{2-δ} has been studied in detail, and the effect of Ce_{0.8}Sn_{0.2}O_{2-δ} on the catalytic performance of Pt for methanol electrooxidation has also been discussed.

2. Experimental

2.1. Chemicals and materials

All chemicals were of analytical grade and used as received. Chloroplatinic acid (IV) hexahydrate (H₂PtCl₆·6H₂O) was purchased from Sino-Platinum Co., Ltd. Cerium (III) nitrate hexahydrate (Ce(NO₃)₃·6H₂O), tin (IV) chloride pentahydrate (SnCl₄·5H₂O), sodium hydroxide (NaOH), ethylene glycol (EG), isopropyl alcohol, ethanol, methanol and sulfuric acid (H₂SO₄) were received from Tianjin Kemiou Chemical Reagent Co., Ltd. Vulcan XC-72 carbon black (BET surface area of ~250 m² g⁻¹) was purchased from Cabot Co. Nafton solution (5 wt.%) was obtained from DuPont Co. Commercial Pt/C catalyst (20 wt.% Pt) was purchased from Johnson Matthey Co. All aqueous solutions were prepared using ultrapure water with a resistivity of 18.2 MΩ cm.

2.2. Preparation of Ce_{0.8}Sn_{0.2}O_{2-δ} solid solution

Ce_{0.8}Sn_{0.2}O_{2-δ} solid solution was synthesized through a simple solvothermal method. In a typical synthesis, quantitative amounts of Ce(NO₃)₃·6H₂O and SnCl₄·5H₂O (total amount of metal ions was 2 mmol, with Ce:Sn = 8:2 molar ratio) were dissolved in 40 mL of ethanol/water (V/V = 1:1) in 100 mL beaker under magnetic stirring. Then, 1.0 mol L⁻¹ NaOH was added into the solution drop by drop until its pH value reached 12. After the mixture was stirred for about 10 min, the light pink suspended solution was transferred into a 50 mL sealed Teflon-lined vessel and heated at 180 °C for 24 h in a furnace. The vessel was then taken out from the furnace and allowed to cool to room temperature naturally. The sandy product was separated by centrifugation and washed repeatedly with deionized water to neutrality. The solid was dried at 80 °C for 12 h in a vacuum oven for later use. For comparison, the un-doped CeO₂ was obtained in the same steps.

2.3. Preparation of Pt/Ce_{0.8}Sn_{0.2}O_{2-δ}–C catalyst

Pt/Ce_{0.8}Sn_{0.2}O_{2-δ}–C catalyst was prepared through a microwave-assisted polyol process as reported by Gu and coworkers [38] with some modification. In detail, the required amounts of Ce_{0.8}Sn_{0.2}O_{2-δ} and Vulcan XC-72 carbon black were initially dispersed in the mixture of EG and isopropanol (V/V = 4:1) in 100 mL beaker and ultrasonicated for 30 min to form a uniform suspension. Then the required volume of 0.1 mol L⁻¹ H₂PtCl₆–EG solution was appended in the suspension. After the mixture was stirred vigorously for 3 h, the pH value of the suspension was adjusted to 12 with dropwise addition of 1 mol L⁻¹ NaOH–EG solution. The beaker was placed the center of a microwave oven (2450 MHz, 700 W) for consecutive heating for 1 min to form Pt/Ce_{0.8}Sn_{0.2}O_{2-δ}–C catalyst. The product was washed repeatedly with acetone and hot deionized water until no Cl⁻ ions were detected. The homemade catalyst was dried at 80 °C for 3 h in a vacuum oven for further characterization and test. For comparison, Pt/CeO₂–C catalyst was prepared through the same synthesis procedure. For all

the catalysts, the Pt loading was 20 wt.%, and the oxide content of hybrid support was 30 wt.%.

2.4. Material characterization

X-ray diffraction (XRD) patterns were obtained with a Bruker D8 diffractometer using Cu-K α ($\lambda = 0.15406$ nm) radiation at step scan 5° from 10° to 80°. The accelerating voltage was 40 kV and the applied current was 20 mA. Raman spectra were collected on a Jobin Yvon HR 800 micro-Raman spectrometer at 632.8 nm. X-ray photoelectron spectroscopy (XPS) was performed by Kratos-AXIS ULTRA DLD, using monochromatic Al Ka (1486.6 eV) radiation as the X-ray source for excitation. The binding energies were referenced to the C 1s line at 284.6 eV from adventitious carbon. High resolution TEM (HRTEM) was performed on a JEOL JEM-2100 electron microscope with an acceleration voltage of 200 kV. Carbon-coated copper grids were used as sample holders for TEM analysis. Energy dispersive X-ray spectrometry (EDX) was obtained with a Hitachi SU8010 microscope. N₂ adsorption/desorption isotherms were measured by a TriStar II 3020 at 77 K. Atomic absorption spectrometry (AAS) was measured by Thermo Elemental SOLAAR-M to determine the accurate content of Pt metal in the sample. Temperature programmed reduction (TPR) measurement was carried out in a conventional setup equipped with a thermal conductivity detector (TCD). The TPR experiments were run in a 10% H₂/Ar stream, with a heating rate of 10 °C min⁻¹. The amount of H₂ uptake during the reduction was measured using a TCD.

2.5. Electrochemical measurements

All electrochemical measurements were carried out on a computer-controlled CHI650E electrochemical analysis instrument in a three-electrode electrochemical cell at 25 °C. A Pt spiral was used as the counter electrode, and the Hg/Hg₂SO₄ electrode (0.71 V relative to reversible hydrogen electrode, RHE) was used as the reference electrode. All potentials reported herein were versus the RHE. The glassy carbon (GC) electrode (4 mm in diameter) coated with the catalyst was used as the working electrode. The working electrode was obtained in the following way: 5 mg of catalyst was dispersed into 2.5 mL ethanol solvent by sonication. Then 5 μ L of catalyst suspension was spread by pipette onto the surface of GC electrode. The subsequent evaporation of ethanol led to the formation of the catalyst layer. Finally, 5 μ L of 5 wt.% Nafion solution was placed on the surface of the GC electrode and dried before electrochemical experiments.

CO stripping voltammetry was performed in 0.5 mol L⁻¹ H₂SO₄ with a scanning rate of 50 mV s⁻¹. The electrochemical surface area (ECSA) of Pt was calculated according to the CO stripping peak assuming the monolayer absorption charge of CO on Pt surface to be 0.42 mC cm⁻² [39]. The electrocatalytic activity of catalysts was examined in 0.5 mol L⁻¹ H₂SO₄ containing 0.5 mol L⁻¹ CH₃OH by cyclic voltammetry (CV) within a potential range from 0.05 V to 1.2 V at 50 mV s⁻¹ and chronoamperometry (CA) curves at the potential of 0.6 V. The long-term durability of the catalysts was carried out by a continuous 1000 potential cycling between 0.05 V and 1.20 V at 50 mV s⁻¹. Electrochemical impedance spectra (EIS) were obtained under a constant voltage at frequencies from 100 KHz to 0.01 Hz with 12 points per decade. Fresh electrolyte solution was used for each electrochemical measurement to ensure reproducible results. The electrolyte solution was deaerated with ultrapure Ar before each experiment.

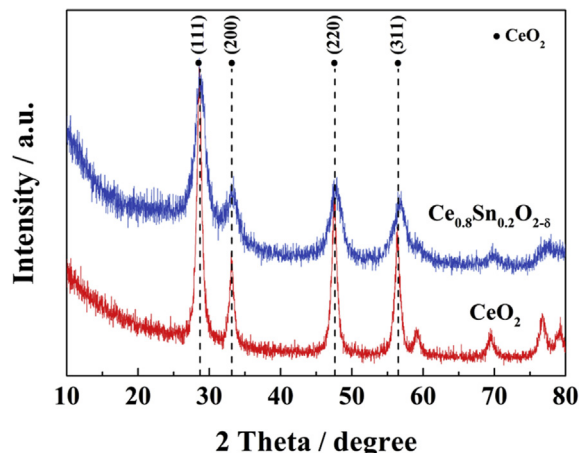


Fig. 1. XRD patterns of $\text{Ce}_{0.8}\text{Sn}_{0.2}\text{O}_{2-\delta}$ and CeO_2 .

3. Results and discussion

3.1. Characterization of $\text{Ce}_{0.8}\text{Sn}_{0.2}\text{O}_{2-\delta}$ solid solution

The XRD patterns of $\text{Ce}_{0.8}\text{Sn}_{0.2}\text{O}_{2-\delta}$ solid solution and un-doped CeO_2 are shown in Fig. 1. All characteristic diffraction peaks for each sample are indexed to face-centered cubic (f.c.c) fluorite structure of CeO_2 . No peaks of SnO or SnO_2 can be found. We can see that the diffraction peak of $\text{Ce}_{0.8}\text{Sn}_{0.2}\text{O}_{2-\delta}$ shifts to higher diffraction angles with the broadening of peak. The calculated lattice parameter for $\text{Ce}_{0.8}\text{Sn}_{0.2}\text{O}_{2-\delta}$ ($a = 0.5370$ nm) is also smaller than that of un-doped CeO_2 ($a = 0.5419$ nm). This is mainly due to the fact that the smaller Sn substitutes the Ce in CeO_2 and the formation of the solid solution [40–42]. The grain size of $\text{Ce}_{0.8}\text{Sn}_{0.2}\text{O}_{2-\delta}$ of 8.1 nm calculated from (220) by using Scherrer's equation [43] is smaller than that of un-doped CeO_2 (about 10.3 nm). The results indicate that the doping of Sn into CeO_2 lattice may inhibit grain growth [32,42].

Fig. 2 depicts the typical Raman spectra of $\text{Ce}_{0.8}\text{Sn}_{0.2}\text{O}_{2-\delta}$ and un-doped CeO_2 . For CeO_2 , the intensive band at about 465 cm⁻¹ is assigned to the Raman-active vibrational mode (F_{2g}) of fluorite-type structure [44]. Obviously, there is a small shift of the band at 465 cm⁻¹ to lower frequency for $\text{Ce}_{0.8}\text{Sn}_{0.2}\text{O}_{2-\delta}$ compared with un-doped CeO_2 , which is due to the decline of the vibration frequency of the metal–anion band and the change of the lattice parameter caused by doping Sn [42]. This is also evidence for the formation of $\text{Ce}_{0.8}\text{Sn}_{0.2}\text{O}_{2-\delta}$ solid solution [45]. In addition, two new Raman band

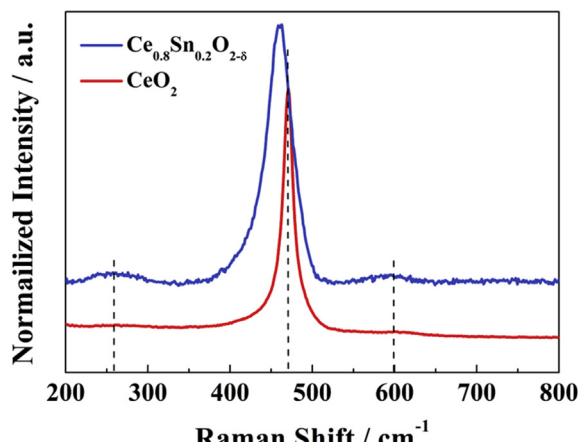


Fig. 2. Raman spectra of $\text{Ce}_{0.8}\text{Sn}_{0.2}\text{O}_{2-\delta}$ and CeO_2 .

at about 260 and 600 cm^{-1} are ascribed to the presence of oxygen vacancies in CeO_2 [46,47]. It is highly possible that the incorporation of Sn into CeO_2 lattice may induce more oxygen vacancies and enhance its OSC, which is favorable for improving the co-catalytic ability of $\text{Ce}_{0.8}\text{Sn}_{0.2}\text{O}_{2-\delta}$ solid solution for methanol electro-oxidation. This deduction will be further verified by the following discussions.

The TEM image of $\text{Ce}_{0.8}\text{Sn}_{0.2}\text{O}_{2-\delta}$ solid solution is shown in Fig. 3(A). It can be seen that the diameter of $\text{Ce}_{0.8}\text{Sn}_{0.2}\text{O}_{2-\delta}$ particles is about 10 nm, which agrees well with the results from XRD patterns. The ring patterns of (111), (200), (220) and (311) can be observed in the selected area of electron diffraction pattern of the $\text{Ce}_{0.8}\text{Sn}_{0.2}\text{O}_{2-\delta}$ (the inset in Fig. 3(A)). HRTEM image (Fig. 3(B)) shows the $\text{Ce}_{0.8}\text{Sn}_{0.2}\text{O}_{2-\delta}$ (111) plane with spacing value of 0.30 nm, which is smaller than that of pure CeO_2 (0.31 nm, JPCDS card No. 34-0394). The decrease of the value can be ascribed to incorporation of Sn into the CeO_2 . The actual Ce:Sn atomic ratio (0.79:0.21) in

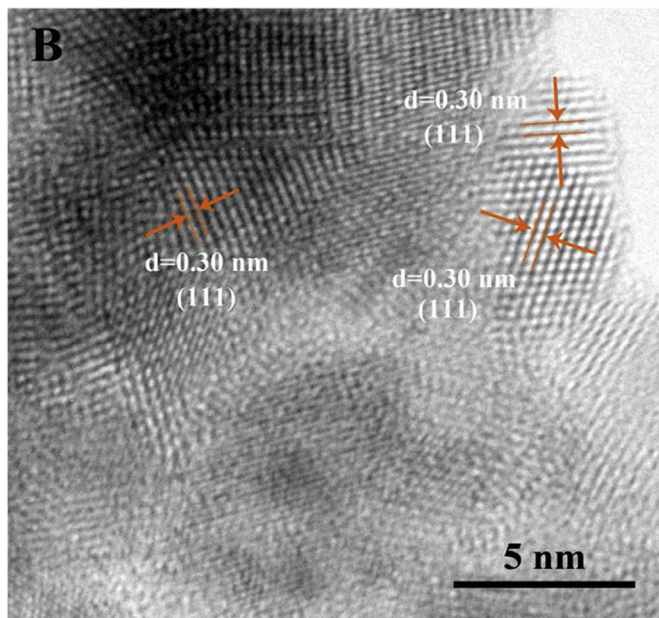
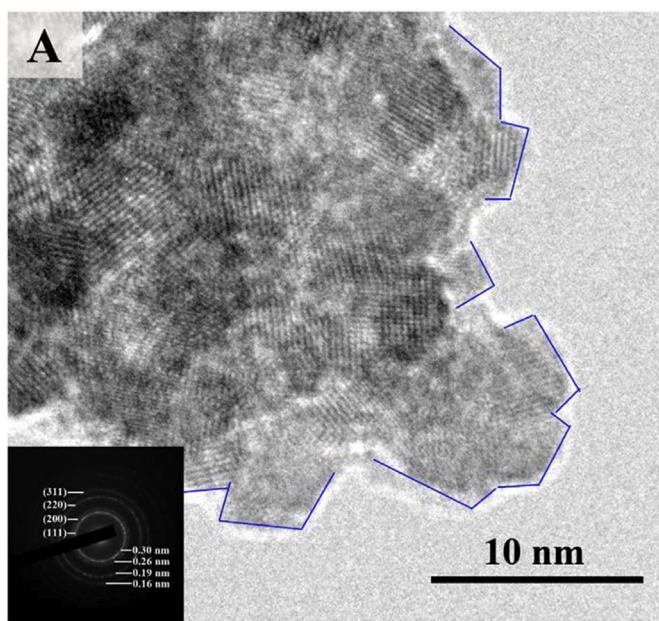


Fig. 3. TEM (A) and HR-TEM (B) images of $\text{Ce}_{0.8}\text{Sn}_{0.2}\text{O}_{2-\delta}$. The inset in part A shows the selected area of electron diffraction pattern of $\text{Ce}_{0.8}\text{Sn}_{0.2}\text{O}_{2-\delta}$.

$\text{Ce}_{0.8}\text{Sn}_{0.2}\text{O}_{2-\delta}$ solid solution can be determined by EDX spectrum (Fig. S1, ESI), the measured result agrees closely with the nominal ratio. N_2 adsorption/desorption isotherms of $\text{Ce}_{0.8}\text{Sn}_{0.2}\text{O}_{2-\delta}$ and un-doped CeO_2 (Fig. S2, ESI) show that the specific surface area of $\text{Ce}_{0.8}\text{Sn}_{0.2}\text{O}_{2-\delta}$ ($128 \text{ m}^2 \text{ g}^{-1}$) is higher than that of un-doped CeO_2 ($89 \text{ m}^2 \text{ g}^{-1}$). The higher specific surface area is favorable for achieving good dispersion of Pt nanoparticles, and consequently, for improving the stability of the catalyst.

Core level Ce 3d spectrum of $\text{Ce}_{0.8}\text{Sn}_{0.2}\text{O}_{2-\delta}$ solid solution is given in Fig. 4(A). Compared with un-doped CeO_2 (Fig. S3, ESI), there is no significant difference between the two spectra. In $\text{Ce}_{0.8}\text{Sn}_{0.2}\text{O}_{2-\delta}$, the Ce 3d_{5/2} and 3d_{3/2} peaks located at 882.3 and 901.0 eV along with the characteristic satellite peaks correspond to the Ce (IV) state [28]. The peaks located at 885.0 and 903.6 eV are characteristic for Ce (III) state [48]. The detail deconvoluted results are listed in Table 1. It can be summarized that both +4 and +3 oxidation states of Ce element coexist in $\text{Ce}_{0.8}\text{Sn}_{0.2}\text{O}_{2-\delta}$. Simultaneously, the proportion of Ce (III) oxidation states in $\text{Ce}_{0.8}\text{Sn}_{0.2}\text{O}_{2-\delta}$ increases as compared with the un-doped CeO_2 . Sn 3d core level spectrum of $\text{Ce}_{0.8}\text{Sn}_{0.2}\text{O}_{2-\delta}$ is shown in Fig. 4(B). The Sn 3d_{5/2} and 3d_{3/2} peaks appear at 486.6 and 494.7 eV, respectively, which correspond to the Sn (IV) state. Compared with SnO_2 (Fig. S4, ESI), the other two peaks at 485.2 and 493.6 eV are typical of Sn (II) [49]. The coexistence of Sn (IV) and Sn (II) is conducive to enhancing the OSC of $\text{Ce}_{0.8}\text{Sn}_{0.2}\text{O}_{2-\delta}$. On the one hand, the substitution of the Sn leads to forming lattice defects in CeO_2 , which promotes the generation of oxygen vacancies [30,40]. On the other hand, the existence of Sn (II) breaks the intrinsic charge balance. In order to maintain the electric neutrality, the valence of Ce changes from +4 to +3, as well as lattice oxygen migrates to the surface and takes off,

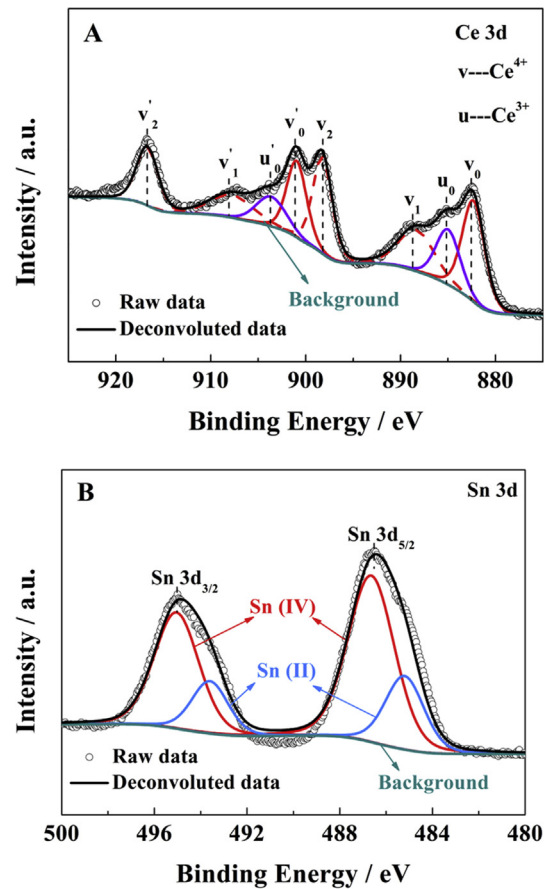


Fig. 4. XPS spectra for Ce 3d (A) and Sn 3d (B) core level regions of $\text{Ce}_{0.8}\text{Sn}_{0.2}\text{O}_{2-\delta}$.

Table 1

Binding energies and surface compositions from deconvolution of XPS spectra for $\text{Ce}_{0.8}\text{Sn}_{0.2}\text{O}_{2-\delta}$.

Sample	Peak	Binding energy (eV)	Species	Relative ratio (%)
$\text{Ce}_{0.8}\text{Sn}_{0.2}\text{O}_{2-\delta}$	Ce 3d	882.3	Ce (IV)	81.0
		888.3	Ce (IV)	
		898.2	Ce (IV)	
		901.0	Ce (IV)	
		907.8	Ce(IV)	
		916.7	Ce (IV)	
		885.0	Ce (III)	19.0
		903.6	Ce (III)	
		486.6	Sn (IV)	73.1
		495.0	Sn (IV)	
	Sn 3d	485.2	Sn (II)	26.9
		493.6	Sn (II)	

leading to the formation of oxygen vacancies on the surface [50,51]. On the basis of above analysis, it is deduced that the doping of Sn into CeO_2 lattice may increase the concentration of oxygen vacancies, which is beneficial to enhance the OSC of $\text{Ce}_{0.8}\text{Sn}_{0.2}\text{O}_{2-\delta}$. This is also confirmed by the O 1s spectrum of $\text{Ce}_{0.8}\text{Sn}_{0.2}\text{O}_{2-\delta}$. As shown in Fig. S5 (ESI), the peak at about 531 eV corresponding to absorption oxygen in $\text{Ce}_{0.8}\text{Sn}_{0.2}\text{O}_{2-\delta}$ is much stronger than that in un-doped CeO_2 , which indicates that $\text{Ce}_{0.8}\text{Sn}_{0.2}\text{O}_{2-\delta}$ has a higher OSC and can supply more oxygen vacancies for reaction [52].

TPR measurement was performed for further verifying the high OSC of $\text{Ce}_{0.8}\text{Sn}_{0.2}\text{O}_{2-\delta}$. The corresponding profiles of $\text{Ce}_{0.8}\text{Sn}_{0.2}\text{O}_{2-\delta}$ and un-doped CeO_2 are shown in Fig. 5(A). Two reduction peaks for un-doped CeO_2 located at about 541 and 926 °C can be ascribed to the reduction of surface and bulk Ce^{4+} species, respectively [53,54]. For $\text{Ce}_{0.8}\text{Sn}_{0.2}\text{O}_{2-\delta}$, two reduction peaks are similar with the profile of CeO_2 . However, all these peaks become larger and shift to lower temperature direction. This change indicates that the dopant Sn may improve the reducibility of Ce^{4+} ion and the migration rate of oxygen species in $\text{Ce}_{0.8}\text{Sn}_{0.2}\text{O}_{2-\delta}$, which facilitate the release of the bulk lattice oxygen to generate oxygen vacancies [55,56]. It is consistent with the results from Raman and XPS analysis. Furthermore, for $\text{Ce}_{0.8}\text{Sn}_{0.2}\text{O}_{2-\delta}$, two new peaks at about 258 and 517 °C may be attributed to the reduction of surface and bulk Sn^{4+} species, respectively [57]. Compared with pure SnO_2 , the two reduction peaks also shift to lower temperature direction, again indicating that the oxygen species in $\text{Ce}_{0.8}\text{Sn}_{0.2}\text{O}_{2-\delta}$ are easier to migrate to generate oxygen vacancies [47,51]. Total OSC value measured from H_2 uptake directly reflect the high OSC of $\text{Ce}_{0.8}\text{Sn}_{0.2}\text{O}_{2-\delta}$. The value of $\text{Ce}_{0.8}\text{Sn}_{0.2}\text{O}_{2-\delta}$ is up to 2714.4 $\mu\text{mol g}^{-1}$, much higher than that of un-doped CeO_2 (Fig. 5(B)).

3.2. Characterization of electrocatalysts

The XRD patterns of commercial Pt/C, Pt/ CeO_2 –C, and Pt/ $\text{Ce}_{0.8}\text{Sn}_{0.2}\text{O}_{2-\delta}$ –C catalysts are given in Fig. 6. The diffraction peak at 2θ of about 24.8° corresponds to the (002) reflections of carbon black. The major peaks located at 2θ of 39.8°, 46.2° and 67.5° are attributed to Pt (111), Pt (200) and Pt (220) characteristic reflection planes of f.c.c structure, respectively. The characteristic peaks of CeO_2 and $\text{Ce}_{0.8}\text{Sn}_{0.2}\text{O}_{2-\delta}$ are also shown in the diffraction patterns of the Pt/ CeO_2 –C and Pt/ $\text{Ce}_{0.8}\text{Sn}_{0.2}\text{O}_{2-\delta}$ –C catalysts, respectively. Obviously, some diffraction peaks of Pt and $\text{Ce}_{0.8}\text{Sn}_{0.2}\text{O}_{2-\delta}$ / CeO_2 could not be identified precisely, because some of them appear in similar 2θ positions [9]. Based on the diffraction peak of Pt (220), the average crystallite size of Pt nanoparticles in Pt/ $\text{Ce}_{0.8}\text{Sn}_{0.2}\text{O}_{2-\delta}$ –C catalyst is estimated to be 2.1 nm, which is smaller than that in Pt/ CeO_2 –C (2.3 nm) and commercial Pt/C catalysts (3.3 nm). These results suggest that the $\text{Ce}_{0.8}\text{Sn}_{0.2}\text{O}_{2-\delta}$ with larger specific surface area is helpful for the dispersion of Pt nanoparticles. There is no

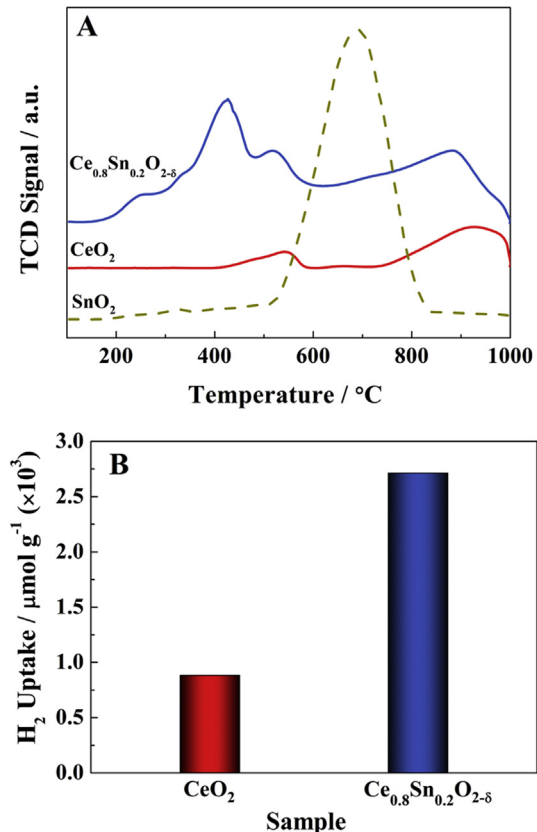


Fig. 5. TPR profiles (A) and total OSC values (B) of $\text{Ce}_{0.8}\text{Sn}_{0.2}\text{O}_{2-\delta}$ and CeO_2 .

obvious shift at the positions of the Pt diffraction peaks in the three catalysts. However, the crystal lattice parameter of Pt in Pt/ $\text{Ce}_{0.8}\text{Sn}_{0.2}\text{O}_{2-\delta}$ –C is 0.3908 nm, which is similar to that in Pt/ CeO_2 –C catalyst (0.3910 nm) and smaller than that in Pt/C catalyst (0.3923 nm). The decrease of crystal lattice parameter indicates the existence of interaction between Pt and oxides [38]. The actual loading contents of Pt in the three catalysts were checked by AAS. The results show that the Pt loading in Pt/ $\text{Ce}_{0.8}\text{Sn}_{0.2}\text{O}_{2-\delta}$ –C, Pt/ CeO_2 –C, and commercial Pt/C catalysts are 18.6 wt.%, 18.7 wt.%, and 19.8 wt.%, respectively.

The HRTEM images of the Pt/ $\text{Ce}_{0.8}\text{Sn}_{0.2}\text{O}_{2-\delta}$ –C catalyst are displayed in Fig. 7. It is visible that most of the spherical Pt nanoparticles with a size of about 2 nm are located at the margin of

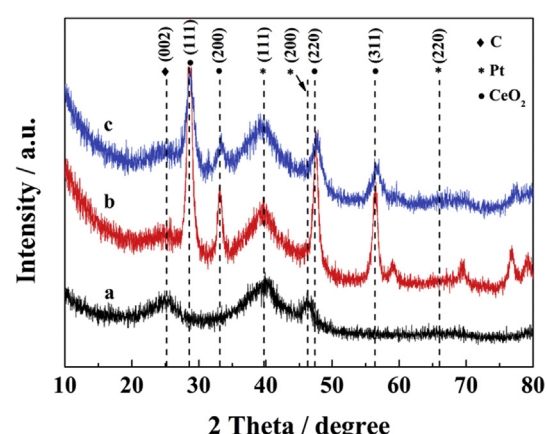


Fig. 6. XRD patterns of commercial Pt/C (a), Pt/ CeO_2 –C (b), and Pt/ $\text{Ce}_{0.8}\text{Sn}_{0.2}\text{O}_{2-\delta}$ –C (c) catalysts.

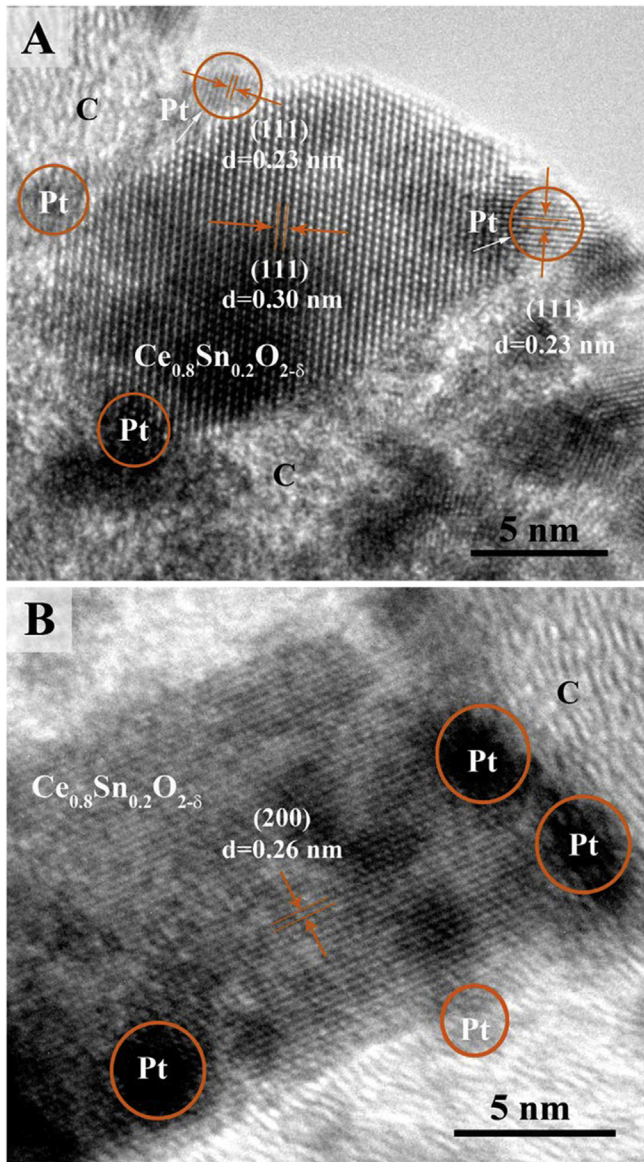


Fig. 7. HRTEM images (A and B) of Pt/Ce_{0.8}Sn_{0.2}O_{2-δ}–C catalyst.

Ce_{0.8}Sn_{0.2}O_{2-δ} deposited on carbon, thus forming the triple junction structure. The lattice fringes of Pt (111) facet as well as Ce_{0.8}Sn_{0.2}O_{2-δ} (111) and (200) facets can also be clearly observed. The formation of the triple junction structure is crucial to achieve the high efficient co-catalytic effect of Ce_{0.8}Sn_{0.2}O_{2-δ} for methanol electrooxidation [58–60].

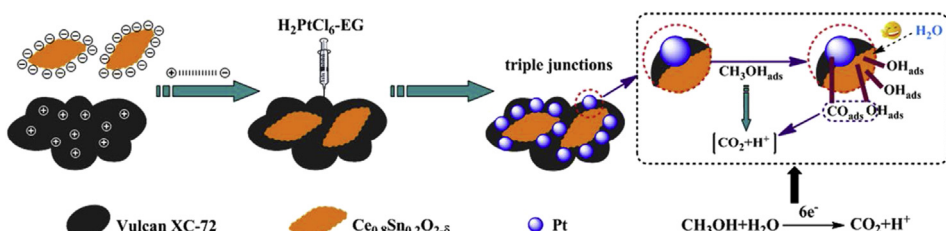
The formation of the special structure of the catalyst is strongly dependent on the preparation process. The detail process is shown

in **Scheme 1**. Ceria-based materials exhibit negative surface charges when the pH value of medium is higher than 7.8 [9,38,61,62]. In our experiment, the synthesis of catalyst was performed in a medium with pH value of 12. Certainly, the Ce_{0.8}Sn_{0.2}O_{2-δ} with high surface area has more negative surface charges, thus being easily adsorbed on carbon black with positive surface charges to form a hybrid support [38]. The hybrid support has a strong hydrophilicity owing to the hydrophilic functional groups from Ce_{0.8}Sn_{0.2}O_{2-δ}. The improvement of hydrophilicity is beneficial for Pt deposition [63,64]. Simultaneously, the Ce_{0.8}Sn_{0.2}O_{2-δ} with abundant negative charges also favors the deposition and dispersion of Pt nanoparticles by a stronger electrostatic interaction [9]. In addition, the reactive solvent EG and isopropanol play an important role in the whole reaction process. The former reduces the [PtCl₆]⁴⁻ to Pt and anchors Pt on hybrid support, while the latter enhances the dispersion of Pt and Ce_{0.8}Sn_{0.2}O_{2-δ} on carbon black [9,38].

XPS was used to testify the surface states of the sample and the interaction between Pt and support. The survey scans of the Pt/Ce_{0.8}Sn_{0.2}O_{2-δ}–C and Pt/CeO₂–C catalysts are shown in **Fig. S6** (ESI). The peaks belong to C 1s, Pt 4f, Ce 3d, Sn 3d, and O 1s signals can be found. The deconvolution of Pt 4f peaks in Pt/Ce_{0.8}Sn_{0.2}O_{2-δ}–C, Pt/CeO₂–C and commercial Pt/C catalysts are shown in **Fig. 8(A)**. The Pt 4f signals of all three catalysts consist of three doublets, all of which have a spin–orbit splitting doublet peaks of 4f_{7/2} and 4f_{5/2} [65]. The deconvoluted results are summarized in **Table 2**. The predominant species in all three catalysts are Pt (0). We can see that the binding energy of Pt (0) peaks for Pt/Ce_{0.8}Sn_{0.2}O_{2-δ}–C and Pt/CeO₂–C catalysts show a positive shift in comparison with the commercial Pt/C catalyst and Pt/C in previous report [66]. The positive shift of Pt (0) binding energy, which was also observed in other reported Pt/CeO₂–C catalysts [38], may be attributed to the change in Pt lattice parameter caused by quantum size effect or the formation of Pt alloy with the metal centers in the oxides. The charge transfer from the support could be excluded on the basis of XPS spectra of Ce 3d and Sn 3d peaks. As shown in **Fig. 8B** and C, Ce 3d and Sn 3d peaks in Pt/Ce_{0.8}Sn_{0.2}O_{2-δ}–C have no obvious shift as compared with those in Ce_{0.8}Sn_{0.2}O_{2-δ}–C. The similar results are also observed in Ce 3d region for Pt/CeO₂–C and CeO₂–C. The possible reason for the lack of shift is due to the response to the lattice strain originated from the deposition of Pt into oxide, which influences the electronic properties [67]. The change of Pt lattice parameter along with the concomitant change of electronic properties suggests the presence of the intensive interaction between Pt and oxide. The interaction is favorable for the improvement of the electrocatalytic properties of catalysts.

3.3. Electrochemical studies

Fig. 9 shows the CO stripping voltammetry curves of the Pt/Ce_{0.8}Sn_{0.2}O_{2-δ}–C, Pt/CeO₂–C and commercial Pt/C catalysts. The Pt/Ce_{0.8}Sn_{0.2}O_{2-δ}–C catalyst exhibits larger peak areas of CO oxidation than other two catalysts. Meanwhile, the onset and oxidation peak



Scheme 1. The synthesis of Pt/Ce_{0.8}Sn_{0.2}O_{2-δ}–C catalyst and the synergistic effect between Pt and Ce_{0.8}Sn_{0.2}O_{2-δ} for methanol electrooxidation.

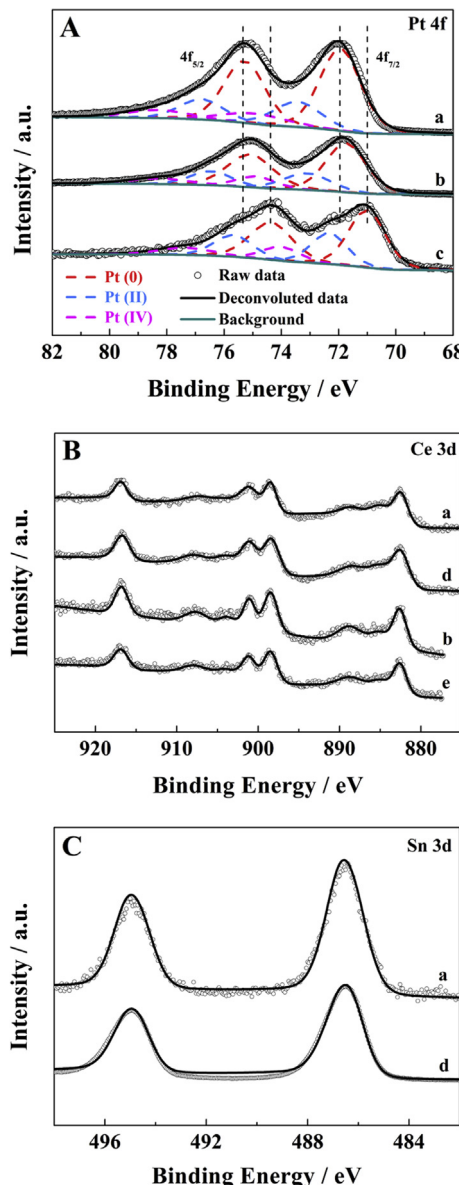


Fig. 8. XPS spectra for Pt 4f (A), Ce 3d (B) and Sn 3d (C) core level regions of the as-prepared samples: Pt/Ce_{0.8}Sn_{0.2}O_{2-δ}-C (a), Pt/CeO₂-C (b), commercial Pt/C (c), Ce_{0.8}Sn_{0.2}O_{2-δ}-C (d) and CeO₂-C (e).

potentials of Pt/Ce_{0.8}Sn_{0.2}O_{2-δ}-C catalyst are lower than those of Pt/CeO₂-C and commercial Pt/C catalysts (in Table 3). This indicates that the Pt/Ce_{0.8}Sn_{0.2}O_{2-δ}-C catalyst is more effective than Pt/CeO₂-C and commercial Pt/C catalysts for electrooxidation of

Table 2

Binding energies and surface compositions from deconvolution of XPS spectra for Pt 4f core level region of Pt/Ce_{0.8}Sn_{0.2}O_{2-δ}-C, Pt/CeO₂-C and commercial Pt/C catalysts.

Sample	Pt (0)		Pt (II)		Pt (IV)	
	Binding energy (eV)	Relative ratio (%)	Binding energy (eV)	Relative ratio (%)	Binding energy (eV)	Relative ratio (%)
Pt/Ce _{0.8} Sn _{0.2} O _{2-δ} -C	71.9	64.5	73.4	22.8	74.9	12.7
	75.3		76.8		78.3	
Pt/CeO ₂ -C	71.7	62.2	73.1	24.3	74.9	13.5
	75.1		76.5		78.2	
Pt/C	71.0	56.5	72.3	29.7	74.0	13.8
	74.3		75.7		77.4	

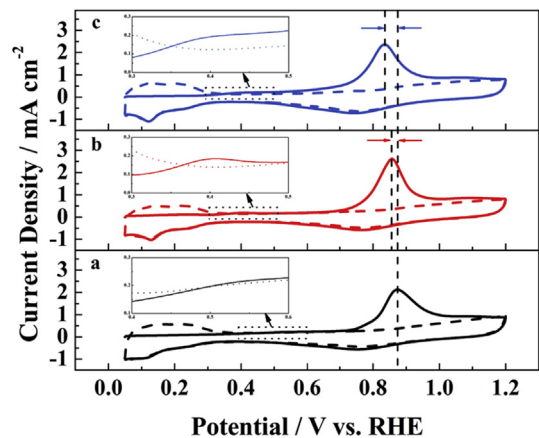


Fig. 9. CO stripping voltammetry curves of commercial Pt/C (a), Pt/CeO₂-C (b) and Pt/Ce_{0.8}Sn_{0.2}O_{2-δ}-C (c) catalysts in 0.5 mol L⁻¹ H₂SO₄ at a scan rate of 50 mV s⁻¹ at 25 °C.

adsorbed CO. The ECSA of Pt nanoparticles defined by the CO stripping area is used to evaluate the electrocatalytic activity of the three catalysts. The results listed in Table 3 reveal that the Pt/Ce_{0.8}Sn_{0.2}O_{2-δ}-C exhibits a larger ECSA than other two catalysts. The larger ECSA implies its great electrocatalytic activity.

The methanol electrooxidation activity of Pt/Ce_{0.8}Sn_{0.2}O_{2-δ}-C, Pt/CeO₂-C and commercial Pt/C catalysts was studied. The CV curves are shown in Fig. 10. The onset potential of methanol oxidation in positive scan can be determined by overlapping the CV curves of in 0.5 mol L⁻¹ H₂SO₄ and in 0.5 mol L⁻¹ H₂SO₄ containing 0.5 mol L⁻¹ CH₃OH [68]. The results in Table 3 show that the onset potential of Pt/Ce_{0.8}Sn_{0.2}O_{2-δ}-C catalyst is 383 mV, which is close to that of Pt/CeO₂-C catalyst and significantly lower than that of commercial Pt/C one. The lower onset potential indicates that the methanol molecules are easily oxidized on the Pt/Ce_{0.8}Sn_{0.2}O_{2-δ}-C catalyst. Besides, the mass activity in positive scan for Pt/Ce_{0.8}Sn_{0.2}O_{2-δ}-C catalyst is up to 502 mA mg⁻¹, which is about 1.2 times higher than that of Pt/CeO₂-C catalyst and 1.4 times higher than that of commercial Pt/C catalyst (in Table 3). Such a significant enhancement can be ascribed to the synergistic effect between Pt and Ce_{0.8}Sn_{0.2}O_{2-δ}, i.e., Ce_{0.8}Sn_{0.2}O_{2-δ} with sufficient OH_{ads} species on the surface promotes the oxidation of poisonous CO_{ads} to release Pt catalyst active sites for further methanol electrooxidation, which has already been demonstrated in the CO stripping voltammetry curves.

So far, the acknowledged mechanism of CO_{ads} electrooxidation process in the Pt–CeO₂–C system is bifunctional mechanism [28,69] represented as follows:



Table 3

Electrochemical characterizations for Pt/Ce_{0.8}Sn_{0.2}O_{2-δ}-C, Pt/CeO₂-C, and commercial Pt/C catalysts.

Sample	Onset potential ^a (mV)	Peak potential ^a (mV)	ECSA ^a (m ² g ⁻¹)	Onset potential ^b (mV)	Mass activity ^b (mA mg _{Pt} ⁻¹)
Pt/Ce _{0.8} Sn _{0.2} O _{2-δ} -C	351	833	96.1	383	502
Pt/CeO ₂ -C	366	856	84.2	388	428
Pt/C	496	873	75.1	533	353

^a Obtained from Fig. 9.

^b Obtained from Fig. 10.

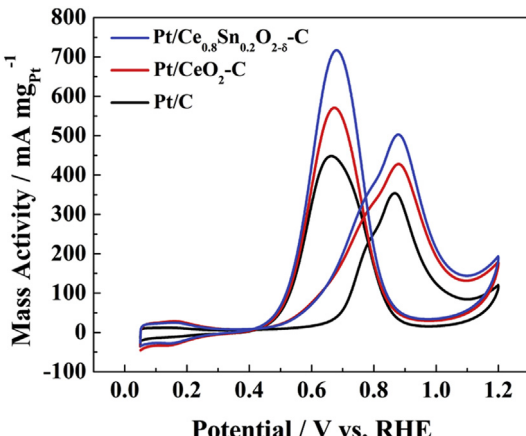
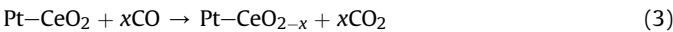


Fig. 10. CV curves of $\text{Pt/Ce}_{0.8}\text{Sn}_{0.2}\text{O}_{2-\delta}\text{-C}$, $\text{Pt/CeO}_2\text{-C}$ and commercial Pt/C catalysts in $0.5 \text{ mol L}^{-1} \text{H}_2\text{SO}_4 + 0.5 \text{ mol L}^{-1} \text{CH}_3\text{OH}$ at a scan rate of 50 mV s^{-1} at 25°C .

and/or



The OH_{ads} species on CeO_2 surface can react with CO_{ads} on Pt surface to produce CO_2 , and the active sites on Pt surface are released for further methanol electrooxidation. Only when Pt nanoparticles and CeO_2 contact with each other, the CO_{ads} on Pt surface can diffuse to Pt– CeO_2 interface and be oxidized by OH_{ads} species [69,70]. Therefore, the resultant number of OH_{ads} species and Pt– CeO_2 interface are particularly important to remove CO_{ads} . In this work, the triple junction structure provides abundant Pt– $\text{Ce}_{0.8}\text{Sn}_{0.2}\text{O}_{2-\delta}$ interfaces for reaction. Also, $\text{Ce}_{0.8}\text{Sn}_{0.2}\text{O}_{2-\delta}$ is able to release sufficient oxygen vacancies as compared with un-doped CeO_2 due to the lattice defects caused by the insertion of Sn into CeO_2 lattice. The increased oxygen vacancies in $\text{Ce}_{0.8}\text{Sn}_{0.2}\text{O}_{2-\delta}$ lead to a higher number of adsorbed OH_{ads} species, which boosts the conversion of CO_{ads} to CO_2 on the $\text{Pt/Ce}_{0.8}\text{Sn}_{0.2}\text{O}_{2-\delta}\text{-C}$ catalyst. The schematic representation of enhanced CO_{ads} electrooxidation mechanism is shown in Scheme 1. It can be summarized that the $\text{Pt/Ce}_{0.8}\text{Sn}_{0.2}\text{O}_{2-\delta}\text{-C}$ catalyst exhibits the best performance for methanol electrooxidation because of the triple junction structure and a higher number of oxygen vacancies on $\text{Ce}_{0.8}\text{Sn}_{0.2}\text{O}_{2-\delta}$.

The methanol electrooxidation activity and stability of the $\text{Pt/Ce}_{0.8}\text{Sn}_{0.2}\text{O}_{2-\delta}\text{-C}$, $\text{Pt/CeO}_2\text{-C}$ and commercial Pt/C catalysts were further evaluated by CA. As shown in Fig. 11, in the initial period, there is a sharp drop in current density for all the three catalysts due to the poisoning of the intermediate species on the catalysts. After 3600 s, the current density at $\text{Pt/Ce}_{0.8}\text{Sn}_{0.2}\text{O}_{2-\delta}\text{-C}$ catalyst exhibits a less current decay as compared with $\text{Pt/CeO}_2\text{-C}$ and commercial Pt/C catalysts. Interestingly, $\text{Pt/Ce}_{0.8}\text{Sn}_{0.2}\text{O}_{2-\delta}\text{-C}$ catalyst shows higher electrocatalytic activity and better stability for methanol electrooxidation than other two catalysts, which is attributed to the efficient removal of the intermediate species benefited from the synergistic effect between Pt and $\text{Ce}_{0.8}\text{Sn}_{0.2}\text{O}_{2-\delta}$.

Another important aspect is to evaluate the charge transport properties of the three catalysts by EIS measurement. In the Nyquist plots, the diameter of the primary semicircle is closely related to the charge reaction resistances (R_{ct}) for methanol electrooxidation [71]. The smaller diameter of the semicircle corresponds to the higher electrocatalytic activity of a catalyst for methanol electrooxidation. As shown in Fig. 12, the diameter of primary semicircle for $\text{Pt/Ce}_{0.8}\text{Sn}_{0.2}\text{O}_{2-\delta}\text{-C}$ catalyst is smaller than that of $\text{Pt/CeO}_2\text{-C}$ and commercial Pt/C catalysts, demonstrating that $\text{Pt/Ce}_{0.8}\text{Sn}_{0.2}\text{O}_{2-\delta}\text{-C}$ catalyst possesses lower R_{ct} . It should be noted that there is an

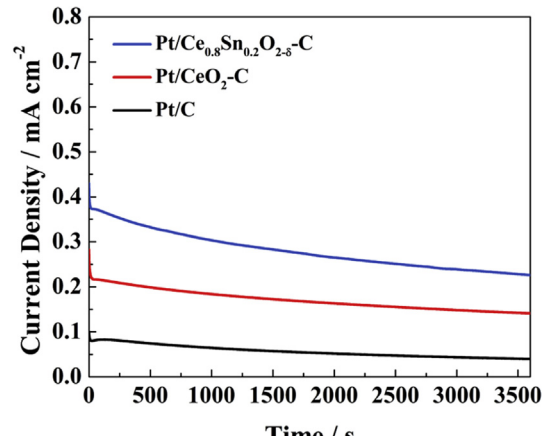


Fig. 11. CA curves of $\text{Pt/Ce}_{0.8}\text{Sn}_{0.2}\text{O}_{2-\delta}\text{-C}$, $\text{Pt/CeO}_2\text{-C}$ and commercial Pt/C catalysts at 0.6 V for 3600 s in $0.5 \text{ mol L}^{-1} \text{H}_2\text{SO}_4 + 0.5 \text{ mol L}^{-1} \text{CH}_3\text{OH}$ at 25°C .

inductive loop at the lowest frequency in all three catalysts, which may be attributed to the pseudo-inductive behavior from the oxidation of CO_{ads} coverage layer [28,71,72]. The $\text{Pt/Ce}_{0.8}\text{Sn}_{0.2}\text{O}_{2-\delta}\text{-C}$ catalyst has the smallest diameter of inductive loop. The Nyquist plots indicate that the reaction rate of methanol electrooxidation for $\text{Pt/Ce}_{0.8}\text{Sn}_{0.2}\text{O}_{2-\delta}\text{-C}$ catalyst is faster than that for other two catalysts, which agrees well with CV and CA results. The possible reason is that the CO_{ads} on Pt active sites from methanol dehydrogenation can be effectively converted on the $\text{Pt/Ce}_{0.8}\text{Sn}_{0.2}\text{O}_{2-\delta}\text{-C}$ catalyst, and consequently, the electrooxidation rate of methanol on the catalyst can be promoted. The intercept of the semicircle on the real axis in the high frequency (the inset in Fig. 12) represents the internal resistances [38]. Pt/C catalyst possesses the least internal resistance. The internal resistance of $\text{Pt/Ce}_{0.8}\text{Sn}_{0.2}\text{O}_{2-\delta}\text{-C}$ catalyst is lower than that of $\text{Pt/CeO}_2\text{-C}$ catalyst, which is owing to the improvement electrical conductivity of CeO_2 caused by doping Sn. The higher electrical conductivity is also conducive to improving the electrocatalytic activity of the catalyst for methanol electrooxidation.

The electrochemical long-term stability behavior of the as-prepared catalysts toward methanol electrooxidation was also investigated by continued potential cycling up to 1000 cycles in $0.5 \text{ mol L}^{-1} \text{H}_2\text{SO}_4$ containing $0.5 \text{ mol L}^{-1} \text{CH}_3\text{OH}$, and the corresponding results are shown in Fig. 13(A)–(C). From the normalized mass activity in Fig. 13(D), the retention rates of mass activity for $\text{Pt/Ce}_{0.8}\text{Sn}_{0.2}\text{O}_{2-\delta}\text{-C}$, $\text{Pt/CeO}_2\text{-C}$ and commercial Pt/C catalysts are 83%, 78% and 65%, respectively. Clearly, $\text{Pt/Ce}_{0.8}\text{Sn}_{0.2}\text{O}_{2-\delta}\text{-C}$ catalyst exhibits the best stability for methanol electrooxidation, which

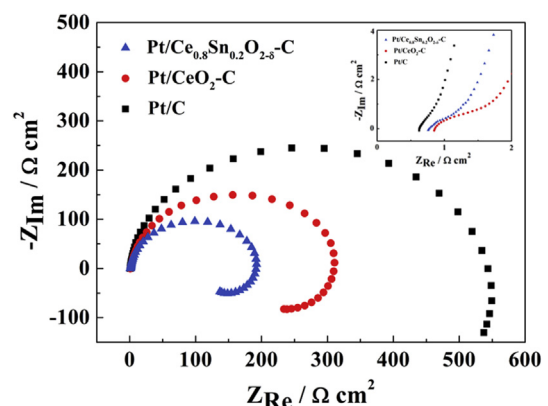


Fig. 12. Nyquist plots of $\text{Pt/Ce}_{0.8}\text{Sn}_{0.2}\text{O}_{2-\delta}\text{-C}$, $\text{Pt/CeO}_2\text{-C}$ and commercial Pt/C catalysts in $0.5 \text{ mol L}^{-1} \text{H}_2\text{SO}_4 + 0.5 \text{ mol L}^{-1} \text{CH}_3\text{OH}$ at 0.6 V at 25°C . The inset shows the amplified part in high frequency regions.

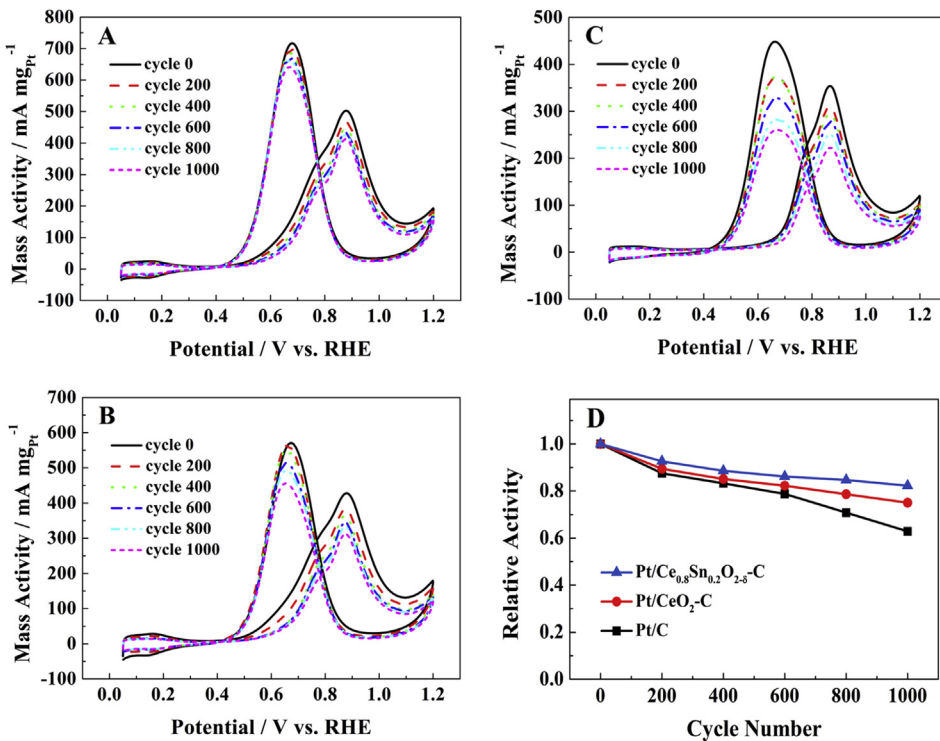


Fig. 13. Continued voltammetry cycles of Pt/Ce_{0.8}Sn_{0.2}O_{2-δ}-C (A), Pt/CeO₂-C (B) and commercial Pt/C catalysts (C) in 0.5 mol L⁻¹ H₂SO₄ at a scan rate of 50 mV s⁻¹ at 25 °C. Relative activity of the three catalysts based on cycle number during stability test (D).

could be ascribed to the strong interaction between Pt and Ce_{0.8}Sn_{0.2}O_{2-δ}.

4. Conclusions

In summary, Ce_{0.8}Sn_{0.2}O_{2-δ} solid solution was synthesized by a simple solvothermal method. The incorporation of Sn into the CeO₂ lattice resulted in a high OSC of final Ce_{0.8}Sn_{0.2}O_{2-δ} sample. The Pt nanoparticles with a small size of about 2 nm were successfully deposited around the Ce_{0.8}Sn_{0.2}O_{2-δ} on the hybrid Ce_{0.8}Sn_{0.2}O_{2-δ}-C support forming a triple junction structure. Pt/Ce_{0.8}Sn_{0.2}O_{2-δ}-C catalyst exhibited a high mass activity of 502 mA mg⁻¹ toward methanol electrooxidation, which was about 1.2 times higher than Pt/CeO₂-C catalyst and 1.4 times higher than commercial Pt/C catalyst. Tolerance to CO and long-term durability of the catalyst were also greatly improved as compared with the other two catalysts. The improvement of electrochemical performance can be attributed to the desirable co-catalytic effect of Ce_{0.8}Sn_{0.2}O_{2-δ}, as well as the synergistic effect from the triple junction in Pt/Ce_{0.8}Sn_{0.2}O_{2-δ}-C catalyst.

Acknowledgments

This research is financially supported by the Natural Science Foundation of Heilongjiang Province of China (Grant No. B201203), the Fund of Department of Education of Heilongjiang Province of China (Grant No. 12521427), and the Heilongjiang Province Postdoctoral Science Foundation (Grant No. LBH-Z11038).

Appendix A. Supplementary data

Supplementary data related to this article can be found at <http://dx.doi.org/10.1016/j.jpowsour.2014.04.137>.

References

- [1] S. Sharma, B.G. Pollet, J. Power Sources 208 (2012) 96–119.
- [2] X. Zhao, M. Yin, L. Ma, L. Liang, C. Liu, J. Liao, T. Lu, W. Xing, Energy Environ. Sci. 4 (2011) 2736–2753.
- [3] E. Antolini, Appl. Catal. B Environ. 88 (2009) 1–24.
- [4] J. Prabhuram, T.S. Zhao, Z.K. Tang, R. Chen, Z.X. Liang, J. Phys. Chem. B 110 (2006) 5245–5252.
- [5] J.Y. Park, J.H. Kim, Y. Seo, D.J. Yu, H. Cho, S.J. Bae, Fuel Cells 12 (2012) 426–438.
- [6] A. Brouzgou, S.Q. Song, P. Tsakarakas, Appl. Catal. B Environ. 127 (2012) 371–388.
- [7] V.J. Wang, D.P. Wilkinson, J. Zhang, Chem. Rev. 111 (2011) 7625–7651.
- [8] K. Matsuoka, K. Miyazaki, Y. Iriyama, K. Kikuchi, T. Abe, Z. Ogumi, J. Phys. Chem. C 111 (2007) 3171–3174.
- [9] S.K. Meher, G.R. Rao, ACS Catal. 2 (2012) 2795–2809.
- [10] B. Abida, L. Chirchi, S. Baranton, T.W. Napporn, C. Morais, J.M. Léger, A. Ghorbel, J. Power Sources 241 (2013) 429–439.
- [11] J. Liu, Z. Zhou, X. Zhao, Q. Xin, G. Sun, B. Yi, Phys. Chem. Chem. Phys. 6 (2004) 134–137.
- [12] M. Zhiani, B. Rezaei, J. Jalili, Int. J. Hydrogen Energy 35 (2010) 9298–9305.
- [13] X.L. Sui, Z.B. Wang, M. Yang, L. Huo, D.M. Gu, G.P. Yin, J. Power Sources 255 (2014) 43–51.
- [14] Y. Shao, J. Liu, Y. Wang, Y. Lin, J. Mater. Chem. 19 (2009) 46–59.
- [15] E. Antolini, E.R. Gonzalez, Appl. Catal. B Environ. 96 (2010) 245–266.
- [16] J. Wang, X. Deng, J. Xi, L. Chen, W. Zhu, X. Qiu, J. Power Sources 170 (2007) 297–302.
- [17] C. Zhou, H. Wang, F. Peng, J. Liang, H. Yu, J. Yang, Langmuir 25 (2009) 7711–7717.
- [18] P. Justin, P. Hari Krishna Charan, G. Ranga Rao, Appl. Catal. B Environ. 100 (2010) 510–515.
- [19] E. Lee, A. Manthiram, J. Phys. Chem. C 114 (2010) 21833–21839.
- [20] C. Feng, T. Takeuchi, M.A. Abdelkareem, T. Tsujiguchi, N. Nakagawa, J. Power Sources 242 (2013) 57–64.
- [21] H. Huang, Q. Chen, M. He, X. Sun, X. Wang, J. Power Sources 239 (2013) 189–195.
- [22] Z. Tang, G. Lu, J. Power Sources 162 (2006) 1067–1072.
- [23] M.S. Saha, R. Li, M. Cai, X. Sun, Electrochim. Solid-State Lett. 10 (2007) B130–B133.
- [24] H. Song, X. Qiu, F. Li, Appl. Catal. A Gen. 364 (2009) 1–7.
- [25] B.Y. Xia, B. Wang, H.B. Wu, Z. Liu, X. Wang, X.W. Lou, J. Mater. Chem. 22 (2012) 16499–16505.
- [26] C. Xu, P.K. Shen, Chem. Commun. (2004) 2238–2239.
- [27] C. Xu, P.K. Shen, J. Power Sources 142 (2005) 27–29.
- [28] M.L. Scibioh, S.K. Kim, E.A. Cho, T.H. Lim, S.A. Hong, H.Y. Ha, Appl. Catal. B Environ. 84 (2008) 773–782.

[29] X. Wang, X. Li, D. Liu, S. Song, H. Zhang, *Chem. Commun.* 48 (2012) 2885–2887.

[30] A. Gupta, U.V. Waghmare, M.S. Hegde, *Chem. Mater.* 22 (2010) 5184–5198.

[31] Z. Hu, B. Li, X.Y. Sun, H. Metiu, *J. Phys. Chem. C* 115 (2011) 3065–3074.

[32] Y. Zuo, X. Huang, L. Li, G. Li, *J. Mater. Chem. A* 1 (2013) 374–380.

[33] E.W. McFarland, H. Metiu, *Chem. Rev.* 113 (2013) 4391–4427.

[34] P. Boizumault-Moriceau, A. Pennequin, B. Grzybowska, Y. Barbaux, *Appl. Catal. A Gen.* 245 (2003) 55–67.

[35] G. Avgouropoulos, T. Ioannides, H. Matralis, *Appl. Catal. B Environ.* 56 (2005) 87–93.

[36] Y. Bai, J. Wu, X. Qiu, J. Xi, J. Wang, J. Li, W. Zhu, L. Chen, *Appl. Catal. B Environ.* 73 (2007) 144–149.

[37] Z. Tang, G. Lu, *Appl. Catal. B Environ.* 79 (2008) 1–7.

[38] D.M. Gu, Y.Y. Chu, Z.B. Wang, Z.Z. Jiang, G.P. Yin, Y. Liu, *Appl. Catal. B Environ.* 102 (2011) 9–18.

[39] Y. Takasu, T. Fujiwara, Y. Murakami, K. Sasaki, M. Oguri, T. Asaki, W. Sugimoto, *J. Electrochem. Soc.* 147 (2000) 4421–4427.

[40] T. Baidya, A. Gupta, P.A. Deshpandey, G. Madras, M.S. Hegde, *J. Phys. Chem. C* 113 (2009) 4059–4068.

[41] P. Borker, A.V. Salkar, *Mater. Sci. Eng. B* 133 (2006) 55–60.

[42] L.L. Li, J. Xu, Q. Yuan, Z.X. Li, W.G. Song, C.H. Yan, *Small* 5 (2009) 2730–2737.

[43] A.S. Deshpande, N. Pinna, P. Beato, M. Antonietti, M. Niederberger, *Chem. Mater.* 16 (2004) 2599–2604.

[44] M. Guo, J. Lu, Y. Wu, Y. Wang, M. Luo, *Langmuir* 27 (2011) 3872–3877.

[45] M.F. Luo, Z.L. Yan, L.Y. Jin, M. He, *J. Phys. Chem. B* 110 (2006) 13068–13071.

[46] R. Kydd, W.Y. Teoh, K. Wong, Y. Wang, J. Scott, Q.H. Zeng, A.B. Yu, J. Zou, R. Amal, *Adv. Funct. Mater.* 19 (2009) 369–377.

[47] X. Yao, C. Tang, Z. Ji, Y. Dai, Y. Cao, F. Gao, L. Dong, Y. Chen, *Catal. Sci. Technol.* 3 (2013) 688–698.

[48] F. Larachi, J. Pierre, A. Adnot, A. Bernis, *Appl. Surf. Sci.* 195 (2002) 236–250.

[49] L.Y. Liang, Z.M. Liu, H.T. Cao, X.Q. Pan, *ACS Appl. Mater. Interfaces* 2 (2010) 1060–1065.

[50] G. Xiao, S. Li, H. Li, L. Chen, *Micropor. Mesopor. Mater.* 120 (2009) 426–431.

[51] X. Yao, Y. Xiong, W. Zou, L. Zhang, S. Wu, X. Dong, F. Gao, Y. Deng, C. Tang, Z. Chen, L. Dong, Y. Chen, *Appl. Catal. B Environ.* 144 (2014) 152–165.

[52] T. Li, G. Xiang, J. Zhuang, X. Wang, *Chem. Commun.* 47 (2011) 6060–6062.

[53] X. Tang, B. Zhang, Y. Li, Y. Xu, Q. Xin, W. Shen, *Catal. Today* 93–95 (2004) 191–198.

[54] M.F. Luo, J.M. Ma, J.Q. Lu, Y.P. Song, Y.J. Wang, *J. Catal.* 246 (2007) 52–59.

[55] Y.Z. Chen, B.J. Liaw, C.W. Huang, *Appl. Catal. A Gen.* 302 (2006) 168–176.

[56] Y.Z. Chen, B.J. Liaw, J.M. Wang, C.T. Huang, *Int. J. Hydrogen Energy* 33 (2008) 2389–2399.

[57] R. Lin, M.F. Luo, Y.J. Zhong, Z.L. Yan, G.Y. Liu, W.P. Liu, *Appl. Catal. A Gen.* 255 (2003) 331–336.

[58] R. Kou, Y. Shao, D. Mei, Z. Nie, D. Wang, C. Wang, V.V. Viswanathan, S. Park, I.A. Aksay, Y. Lin, Y. Wang, J. Liu, *J. Am. Chem. Soc.* 133 (2011) 2541–2547.

[59] L. Yu, J. Xi, *Int. J. Hydrogen Energy* 37 (2012) 15938–15947.

[60] J. Yang, Y. Xie, R. Wang, B. Jiang, C. Tian, G. Mu, J. Yin, B. Wang, H. Fu, *ACS Appl. Mater. Interfaces* 5 (2013) 6571–6579.

[61] A. Bumajdad, M.I. Zaki, J. Eastoe, L. Pasupulety, *Langmuir* 20 (2004) 11223–11233.

[62] C. Pan, D. Zhang, L. Shi, *J. Solid State Chem.* 181 (2008) 1298–1306.

[63] Y.M. Volkovich, V.E. Sosenkin, V.S. Bagotsky, *J. Power Sources* 195 (2010) 5429–5441.

[64] A. Kongkanand, S. Kuwabata, G. Girishkumar, P. Kamat, *Langmuir* 22 (2006) 2392–2396.

[65] K.W. Park, J.H. Choi, B.K. Kwon, S.A. Lee, Y.E. Sung, H.Y. Ha, S.A. Hong, H. Kim, A. Wieckowski, *J. Phys. Chem. B* 106 (2002) 1869–1877.

[66] L. Ma, X. Zhao, F. Si, C. Liu, J. Liao, L. Liang, W. Xing, *Electrochim. Acta* 55 (2010) 9105–9112.

[67] L. Timperman, A. Lewera, W. Vogel, N. Alonso-Vante, *Electrochim. Commun.* 12 (2010) 1772–1775.

[68] J. Cao, Z. Chen, J. Xu, W. Wang, Z. Chen, *Electrochim. Acta* 88 (2013) 184–192.

[69] H. Yuan, D. Guo, X. Li, L. Yuan, W. Zhu, L. Chen, X. Qiu, *Fuel Cells* 9 (2009) 121–127.

[70] J. Wang, J. Xi, Y. Bai, Y. Shen, J. Sun, L. Chen, W. Zhu, X. Qiu, *J. Power Sources* 164 (2007) 555–560.

[71] G. Wu, L. Li, B.Q. Xu, *Electrochim. Acta* 50 (2004) 1–10.

[72] H. Yuan, D. Guo, X. Qiu, W. Zhu, Li Chen, *J. Power Sources* 188 (2009) 8–13.